

Quantum calcium-ion interactions with EEG

Lester Ingber^{1,†,‡} 

¹ Lester Ingber Research; ingber@alumni.caltech.edu [1]

† Current address: Lester Ingber Research, Ashland, OR, USA

Received: date; Accepted: date; Published: date

Abstract: **Background:** Previous papers have developed a statistical mechanics of neocortical interactions (SMNI) fit to short-term memory and EEG data. Adaptive Simulated Annealing (ASA) has been developed to perform fits to such nonlinear stochastic systems. An N-dimensional path-integral algorithm for quantum systems, qPATHINT, has been developed from classical PATHINT. Previous papers applied qPATHINT to two systems, in neocortical interactions and financial options. **Methods:** Methods of mathematical-physics for optimization and for path integrals in classical and quantum spaces are used for this project. Studies using supercomputer resources tested various dimensions for their scaling limits. In this paper the quantum path-integral is used to derive a closed-form analytic solution at arbitrary time that is used to calculate interactions with classical-physics SMNI interactions among scales. **Results:** The mathematical-physics and computer parts of the study are successful, in that there is modest improvement of cost/objective functions used to fit EEG data using these models. **Conclusion:** This project points to directions for more detailed calculations using more EEG data and qPATHINT at each time slice to propagate quantum calcium waves, synchronized with PATHINT propagation of classical SMNI.

Keywords: quantum mechanics; EEG; short term memory; astrocytes; neocortical dynamics; vector potential

Funding: The author thanks the Extreme Science and Engineering Discovery Environment (XSEDE.org), for supercomputer grants since February 2013, starting with Electroencephalographic field influence on calcium momentum waves, one under PHY130022 and two under TG-MCB140110. The current grant under TG-MCB140110, Quantum path-integral qPATHTREE and qPATHINT algorithms, was started in 2017, and renewed through December 2018.

1. Introduction

This project calculates quantum Ca^{2+} interactions with EEG. In this paper, EEG is synonymous with large-scale neocortical firings during attentional tasks as measured by large-amplitude electroencephalographic (EEG) recordings. In this paper, only very specific calcium ions, Ca^{2+} , are considered, those arising from regenerative calcium waves generated at tripartite neuron-astrocyte-neuron synapses.

Section 2 gives the background of the main model used, Statistical Mechanics of Neocortical Interactions (SMNI).

Section 3 gives new results of inclusion of quantum-mechanical interactions of Ca^{2+} wave-packets with EEG.

Section 4 gives some applications of this project.

Section 5 gives the conclusion.

Appendix A describes the code Adaptive Simulated Annealing (ASA), used for optimization of many systems – fitting models to real data, e.g., fits to EEG data reported here.

Appendix B give the development of path-integral codes, PATHINT and qPATHINT, used for propagation of conditional probabilities and quantum-mechanical wave-functions, as reported here.

2. Statistical Mechanics of Neocortical Interactions (SMNI)

This section paraphrases previous papers by this author, including a recent paper [1].

SMNI has been developed since 1981, scaling aggregate synaptic interactions to neuronal firings, up to minicolumnar-macrocolumnar columns of neurons to mesocolumnar dynamics, up to columns of neuronal firings, up to regional macroscopic sites [2–7].

SMNI has calculated agreement/fits with experimental data from various aspects of neocortical interactions, e.g., properties of short-term memory (STM) [8], including its capacity (auditory 7 ± 2 and visual 4 ± 2) [9,10], duration, stability, primacy versus recency rule, as well other phenomenon, e.g., Hick's law [11–13], interactions within macrocolumns calculating rotation of images, etc [3–7]. SMNI scaled mesocolumns across neocortical regions to fit EEG data [8,14,15].

2.1. Model of Models (MOM)

Deep Learning (DL) has invigorated AI approaches to parsing data in complex systems, often to develop control processes of these systems. A couple of decades ago, Neural Net AI approaches fell out of favor when concerns were apparent that such approaches offered little guidance to explain the "why" or "how" such algorithms worked to process data, e.g., contexts which were deemed important to deal with future events and outliers, etc.

The success of DL has overshadowed these concerns. However, that should not diminish their importance, especially if such systems are placed in positions to affect lives and human concerns; humans are ultimately responsible for structures they build.

An approach to dealing with these concerns can be called Model of Models (MOM). An argument in favor of MOM is that humans over thousands of years have developed models of reality across many disciplines, e.g., ranging over Physics, Biology, Mathematics, Economics, etc.

A good use of DL might be to process data for a given system in terms of a collection of models, then again use DL to process the models over the same data to determine a superior model of models (MOM). Eventually, large DL (quantum) machines could possess a database of hundreds or thousands of models across many disciplines, and directly find the best (hybrid) MOM for a given system.

In particular, SMNI offers a reasonable model upon which to further develop MOM, wherein multiple scales of observed interactions are developed. This is just one example of how physics modeling and computational physics can be used to better understand complex systems. Fig. 1 depicts this model [4].

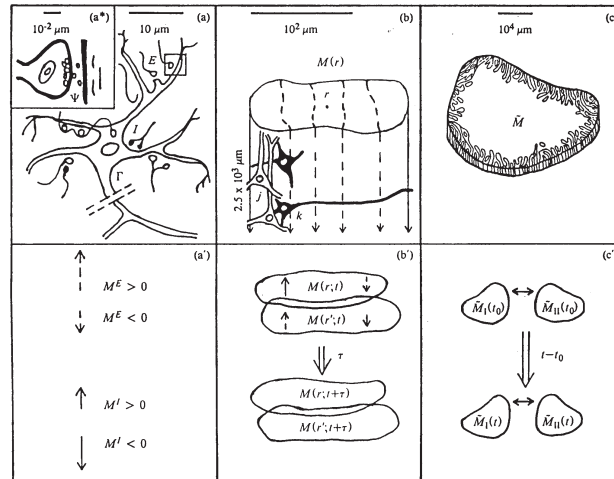


Figure 1 illustrates three SMNI biophysical scales [3,4]: (a)-(a*)-(a') microscopic neurons; (b)-(b') mesocolumnar domains; (c)-(c') macroscopic regions.

(a*): synaptic inter-neuronal interactions, scaled up to mesocolumns, phenomenologically described by the mean and variance of a distribution Ψ (a): intraneuronal transmissions phenomenologically described by the mean and variance of Γ (a'): collective mesocolumnar-averaged inhibitory (I) and excitatory (E) neuronal firings M (b): vertical organization of minicolumns including their horizontal layers, yielding a physiological entity, the mesocolumn (b'): overlapping mesocolumns at locations r and r' from times t and $t + \tau$, τ on the order of 10 msec (c): macroscopic regions of neocortex arising from many mesocolumnar domains (c'): regions coupled by long-ranged interactions

2.1.1. Ideas by Statistical Mechanics

A project sympathetic to this MOM context was proposed as Ideas by Statistical Mechanics (ISM) [16–18]. using ASA [19–21] to fit parameters of a generic nonlinear multivariate colored-noise Gaussian-Markovian short-time conditional probability distribution to data, useful for many systems.

Models developed using ASA have been applied in many contexts across many systems [22], including applications to neural networks [23].

Many of these ASA applications have used Ordinal representations of features, to permit parameterization of their inclusion into models, quite similar in spirit to DL.

ASA can be used again in the expanded context of MOM. This is suggested as a first step in a new discipline to which MOM is to be applied, to help develop a range of parameters useful for DL, as

DL by itself may get stuck in non-ideal local minima of the importance-sampled space. Then, after a reasonable range of models is found, DL can take over to permit much more efficient and accurate development of MOM for a given discipline/system.

2.2. SMNI Development

2.2.1. Synaptic Interactions

The short-time conditional probability distribution of firing of a given neuron firing given just-previous firings of other neurons is calculated from chemical and electrical intra-neuronal interactions [3,4]. Given its previous interactions with k neurons within τ_j of 5-10 msec, the conditional probability that neuron j fires ($\sigma_j = +1$) or does not fire ($\sigma_j = -1$) is

$$p_{\sigma_j} = \Gamma\Psi = \frac{\exp(-\sigma_j F_j)}{\exp(F_j) + \exp(-F_j)}$$

$$F_j = \frac{V_j - \sum_k a_{jk}^* v_{jk}}{(\pi \sum_{k'} a_{jk'}^* (v_{jk'}^2 + \phi_{jk'}^2))^{1/2}}$$

$$a_{jk} = \frac{1}{2} A_{|jk|} (\sigma_k + 1) + B_{jk} \quad (1)$$

The contribution to polarization achieved at an axon given activity at a synapse, taking into account averaging over different neurons, geometries, etc., is given by Γ , the ‘‘intra-neuronal’’ probability distribution. Ψ is the ‘‘inter-neuronal’’ probability distribution, of thousands of quanta of neurotransmitters released at one neuron’s postsynaptic site effecting a (hyper-)polarization at another neuron’s presynaptic site, taking into account interactions with neuromodulators, etc. This development holds for Γ Poisson, and for Ψ Poisson or Gaussian.

V_j is the depolarization threshold in the somatic-axonal region. v_{jk} is the induced synaptic polarization of E or I type at the axon, and ϕ_{jk} is its variance. The efficacy a_{jk} is a sum of A_{jk} from the connectivity between neurons, activated if the impinging k -neuron fires, and B_{jk} from spontaneous background noise. The efficacy is related to the inverse conductivity across synaptic gaps.

2.2.2. Neuronal Interactions

Aggregation up to the mesoscopic scale from the microscopic synaptic scale uses mesoscopic probability P

$$P = \prod_G P^G [M^G(r; t + \tau) | M^{\bar{G}}(r'; t)]$$

$$= \sum_{\sigma_j} \delta \left(\sum_{j \in E} \sigma_j - M^E(r; t + \tau) \right) \delta \left(\sum_{j \in I} \sigma_j - M^I(r; t + \tau) \right) \prod_j^N p_{\sigma_j} \quad (2)$$

M represents a mesoscopic scale of columns of N neurons, with subsets E and I , represented by p_{q_i} . The ‘‘delta’’-functions δ -constraint represents an aggregate of many neurons in a column. G is used to represent excitatory (E) and inhibitory (I) contributions. \bar{G} designates contributions from both E and I .

The path integral is derived in terms of mesoscopic Lagrangian L . The short-time distribution of firings in a minicolumn, given its just previous interactions with all other neurons in its macrocolumn, is thereby defined.

2.2.3. Columnar Interactions

In the prepoint (Ito) representation the SMNI Lagrangian L is

$$\begin{aligned}
L &= \sum_{G,G'} (2N)^{-1} (\dot{M}^G - g^G) g_{GG'} (\dot{M}^{G'} - g^{G'}) / (2N\tau) - V' \\
g^G &= -\tau^{-1} (M^G + N^G \tanh F^G) \\
g^{GG'} &= (g_{GG'})^{-1} = \delta_{G'}^{G'} \tau^{-1} N^G \operatorname{sech}^2 F^G \\
g &= \det(g_{GG'}) \tag{3}
\end{aligned}$$

The threshold factor F^G is derived as

$$\begin{aligned}
F^G &= \sum_{G'} \frac{v^G + v^{\dagger E'}}{((\pi/2)[(v_{G'}^G)^2 + (\phi_{G'}^G)^2](\delta^G + \delta^{\dagger E'}))^{1/2}} \\
v^G &= V^G - a_{G'}^G v_{G'}^G N^{G'} - \frac{1}{2} A_{G'}^G v_{G'}^G M^{G'}, v^{\dagger E'} = -a_{E'}^{\dagger E} v_{E'}^E N^{\dagger E'} - \frac{1}{2} A_{E'}^{\dagger E} v_{E'}^E M^{\dagger E'} \\
\delta^G &= a_{G'}^G N^{G'} + \frac{1}{2} A_{G'}^G M^{G'}, \delta^{\dagger E'} = a_{E'}^{\dagger E} N^{\dagger E'} + \frac{1}{2} A_{E'}^{\dagger E} M^{\dagger E'} \\
a_{G'}^G &= \frac{1}{2} A_{G'}^G + B_{G'}^G, a_{E'}^{\dagger E} = \frac{1}{2} A_{E'}^{\dagger E} + B_{E'}^{\dagger E} \tag{4}
\end{aligned}$$

where $A_{G'}^G$ is the columnar-averaged direct synaptic efficacy, $B_{G'}^G$ is the columnar-averaged background-noise contribution to synaptic efficacy. The “ \dagger ” parameters arise from regional interactions across many macrocolumns.

2.2.4. SMNI Parameters From Experiments

All values of parameters and their bounds are taken from experimental data, not arbitrarily fit to specific phenomena.

$N^G = \{N^E = 160, N^I = 60\}$ was set for visual neocortex, $\{N^E = 80, N^I = 30\}$ was set for all other neocortical regions, $M^{G'}$ and $N^{G'}$ in F^G are afferent macrocolumnar firings scaled to efferent minicolumnar firings by $N/N^* \approx 10^{-3}$. N^* is the number of neurons in a macrocolumn, about 10^5 . V' includes nearest-neighbor mesocolumnar interactions. τ is usually considered to be on the order of 5-10 ms.

Other values also are consistent with experimental data, e.g., $V^G = 10$ mV, $v_{G'}^G = 0.1$ mV, $\phi_{G'}^G = 0.03^{1/2}$ mV.

Nearest-neighbor interactions among columns give dispersion relations that were used to calculate speeds of visual rotation [3,4].

The wave equation cited by EEG theorists, permitting fits of SMNI to EEG data [24], was derived using the variational principle applied to the SMNI Lagrangian.

This creates an audit trail from synaptic parameters to the statistically averaged regional Lagrangian.

2.3. Previous Applications

2.3.1. Verification of basic SMNI Hypothesis

The core SMNI hypothesis first developed circa 1980 [2-4] is that highly synchronous patterns of neuronal firings in fact process high-level information. Only since 2012 has this hypothesis been verified experimentally [25,26].

2.3.2. SMNI Calculations of Short-Term Memory (STM)

SMNI calculations agree with observations [1,3–8,12,14,27–34]: This list includes:

- capacity (auditory 7 ± 2 and visual 4 ± 2) [5]
- duration [6]
- stability [6]
- primacy versus recency rule [6,35]
- Hick's law (reaction time and g factor) [12]
- nearest-neighbor minicolumnar interactions => rotation of images [3,4]
- derivation of basis for EEG [24,36]

2.3.3. Three Basic SMNI Models

Three basic models were developed by slightly changing the background firing component of the columnar-averaged efficacies B_G^G , within experimental ranges, which modify F^G threshold factors to yield in the conditional probability:

- (a) case EC, dominant excitation subsequent firings
- (b) case IC, inhibitory subsequent firings
- (c) case BC, balanced between EC and IC

This is consistent with experimental evidence of shifts in background synaptic activity under conditions of selective attention [37,38], This enables a Centering Mechanism (CM) on case BC, giving BC' , wherein the numerator of F^G only has terms proportional to $M^{E'}$, $M^{I'}$ and $M^{\ddagger E'}$, i.e., zeroing other constant terms by resetting the background parameters $B_{G'}^G$, still within experimental ranges. This brings in a maximum number of minima into the physical firing M^G -space, due to the minima of the new numerator in being in a parabolic trough defined by

$$A_E^E M^E - A_I^E M^I = 0 \quad (5)$$

about which nonlinearities develop multiple minima identified with STM phenomena.

In current projects a Dynamic CM (DCM) model is used, resetting $B_{G'}^G$ every few epochs of τ . Such changes in background synaptic activity on such time scales are seen during attentional tasks [37].

2.3.4. PATHINT STM

The evolution of a Balanced Centered model (BC) after 500 foldings of $\Delta t = 0.01$, 5 unit of relaxation time τ , exhibits the existence of ten well developed peaks. These peaks are identified with possible trappings of firing patterns.

This describes the “ 7 ± 2 ” rule, as calculated by SMNI PATHINT in Fig. 2 [39].

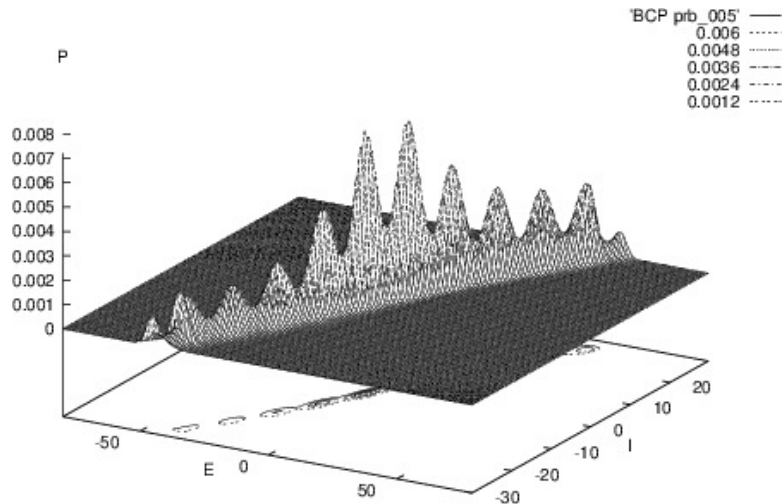


Figure 2 illustrates SMNI STM Model BC at the evolution at 5τ [39].

2.3.5. PATHINT STM Visual

The evolution of a Balanced Centered Visual model (BCV) after 1000 foldings of $\Delta t = 0.01$, 10 unit of relaxation time τ , exhibits the existence of four well developed peaks. These peaks are identified with possible trappings of firing patterns. Other peaks at lower scales are clearly present, numbering on the same order as in the BC' model, as the strength in the original peaks dissipates throughout firing space, but these are much smaller and therefore much less probable to be accessed.

This describes the " 4 ± 2 " rule for visual STM, as calculated by SMNI PATHINT in Fig. 3 [39].

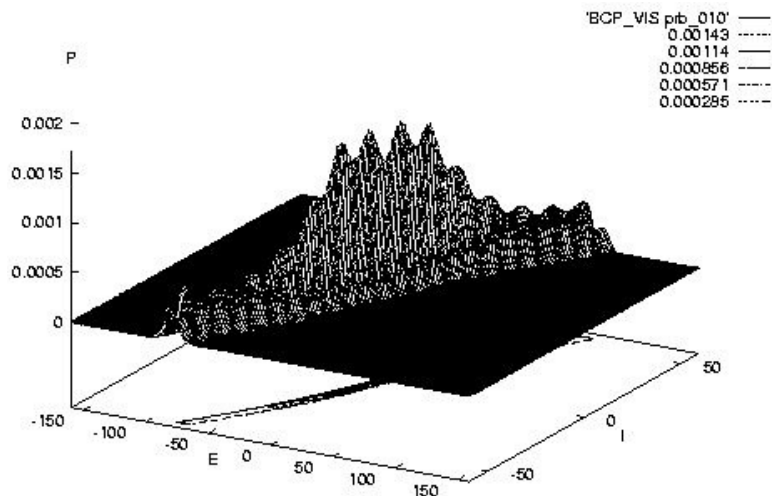


Figure 3 illustrates SMNI STM Model BCV at the evolution at 10τ [39].

2.4. Tripartite Synaptic Interactions

The human brain contains over 10^{11} cells, about half of which are neurons. The other half are glial cells. Astrocytes comprise a good fraction of glial cells, possibly the majority. Many papers examine the influence of astrocytes on synaptic processes [40–48].

<http://www.astrocyte.info> claims they are the most numerous cells in the human brain. Unlike the previous ideology of astrocytes being “filler” cells, they are very active in the central nervous system and greatly outnumber neurons,

Glutamate release from astrocytes through a Ca^{2+} -dependent mechanism can activate receptors at the presynaptic terminals. Intercellular calcium waves (ICWs) may travel over hundreds of astrocytes propagating over many neuronal synapses. ICWs contribute to control synaptic activity. Glutamate is released in a regenerative manner, with subsequent cells that are involved in the calcium wave releasing additional glutamate [49].

$[\text{Ca}^{2+}]$ (concentrations of Ca^{2+}) affect increased release probabilities at synaptic sites, by enhancing the release of gliotransmitters. (Free Ca^{2+} waves are considered here, not intracellular astrocyte calcium waves in situ which also increase neuronal firings.)

As described below, these free regenerative Ca^{2+} waves, arising from astrocyte-neuron interactions, couple to the magnetic vector potential \mathbf{A} produced by highly synchronous collective firings, e.g., during selective attention tasks, as measured by EEG.

2.4.1. Canonical Momentum $\mathbf{\Pi} = \mathbf{p} + q\mathbf{A}$

As derived in the Feynman (midpoint) representation of the path integral, the canonical momentum, $\mathbf{\Pi}$, defines the dynamics of a moving particle with momentum \mathbf{p} in an electromagnetic field. In SI units,

$$\mathbf{\Pi} = \mathbf{p} + q\mathbf{A} \quad (6)$$

where $q = -2e$ for Ca^{2+} , e is the magnitude of the charge of an electron = 1.6×10^{-19} C (Coulomb), and \mathbf{A} is the electromagnetic vector potential. (In Gaussian units $\mathbf{\Pi} = \mathbf{p} + q\mathbf{A}/c$, where c is the speed of light.) \mathbf{A} represents three components of a 4-vector.

2.4.2. Vector Potential of Wire

A columnar firing state is modeled as a wire/neuron with current \mathbf{I} measured in A = Amperes = C/s,

$$\mathbf{A}(t) = \frac{\mu}{4\pi} \int \frac{dr}{r} \mathbf{I} \quad (7)$$

along a length z observed from a perpendicular distance r from a line of thickness r_0 . If far-field retardation effects are neglected, this yields

$$\mathbf{A} = \frac{\mu}{4\pi} \mathbf{I} \log\left(\frac{r}{r_0}\right) \quad (8)$$

where μ is the magnetic permeability in vacuum $= 4\pi 10^{-7}$ H/m (Henry/meter). Note the insensitive log dependence on distance.

The contribution to \mathbf{A} includes minicolumnar lines of current from hundreds to thousands of macrocolumns, within a region not so large to include many convolutions, but still contributing to large synchronous bursts of EEG.

Electric \mathbf{E} and magnetic \mathbf{B} fields, derivatives of \mathbf{A} with respect to r , do not possess this logarithmic insensitivity to distance, and therefore they do not linearly accumulate strength within and across macrocolumns.

Estimates of contributions from synchronous firings to P300 measured on the scalp are tens of thousands of macrocolumns spanning 100 to 100's of cm^2 . Electric fields generated from a minicolumn may fall by half within 5-10 mm, the range of several macrocolumns.

2.4.3. Effects of Vector Potential on Momenta

The momentum \mathbf{p} for a Ca^{2+} ion with mass $m = 6.6 \times 10^{-26}$ kg, speed on the order of $50 \mu\text{m/s}$ to $100 \mu\text{m/s}$, is on the order of 10^{-30} kg-m/s. Molar concentrations of Ca^{2+} waves, comprised of tens of thousands of free ions representing about 1% of a released set, most being buffered, are within a range of about $100 \mu\text{m}$ to as much as $250 \mu\text{m}$, with a duration of more than 500 ms, and with $[\text{Ca}^{2+}]$ ranging from 0.1-5 μM ($\mu\text{M} = 10^{-3}$ mol/ m^3).

The magnitude of the current is taken from experimental data on dipole moments $\mathbf{Q} = |\mathbf{I}|\hat{\mathbf{z}}$ where $\hat{\mathbf{z}}$ is the direction of the current \mathbf{I} with the dipole spread over z . \mathbf{Q} ranges from 1 pA-m $= 10^{-12}$ A-m for a pyramidal neuron [50], to 10^{-9} A-m for larger neocortical mass [51]. These currents give rise to $q\mathbf{A} \approx 10^{-28}$ kg-m/s. The velocity of a Ca^{2+} wave can be ≈ 20 - $50 \mu\text{m/s}$. In neocortex, a typical Ca^{2+} wave of 1000 ions, with total mass $m = 6.655 \times 10^{-23}$ kg times a speed of ≈ 20 - $50 \mu\text{m/s}$, gives $\mathbf{p} \approx 10^{-27}$ kg-m/s.

Taking 10^4 synchronous firings in a macrocolumn, leads to a dipole moment $|\mathbf{Q}| = 10^{-8}$ A-m. Taking z to be $10^2 \mu\text{m} = 10^{-4}$ m, a couple of neocortical layers, gives $|q\mathbf{A}| \approx 2 \times 10^{-19} \times 10^{-7} \times 10^{-8}/10^{-4} = 10^{-28}$ kg-m/s,

2.4.4. Reasonable Estimates

Estimates used here for \mathbf{Q} come from experimental data. These include shielding and material effects. When coherent activity among many macrocolumns associated with STM is considered, $|\mathbf{A}|$ may be much larger. Since Ca^{2+} waves influence synaptic activity, there is direct coherence between these waves and the activity of \mathbf{A} .

Classical physics calculates $q\mathbf{A}$ from macroscopic EEG to be on the order of 10^{-28} kg-m/s, while the momentum \mathbf{p} of a Ca^{2+} ion is on the order of 10^{-30} kg-m/s. This numerical comparison demonstrates the possible importance of the influence of \mathbf{A} on \mathbf{p} at classical scales.

This project fits the SMNI model to EEG data. Direct calculations in classical and quantum physics support the concepts presented here, e.g., that ionic calcium momentum-wave effects among neuron-astrocyte-neuron tripartite synapses modify background SMNI parameters and create feedback between ionic/quantum and macroscopic scales [8,29-34].

2.5. Comparing Testing Data with Training Data

Using EEG data from <http://physionet.nlm.nih.gov/pn4/erpbc1>, SMNI was fit to highly synchronous waves (P300) during attentional tasks, for each of 12 subjects, it was possible to find 10 Training runs and 10 Testing runs [52,53].

Spline-Laplacian transformations on the EEG potential Φ are proportional to the SMNI M^G firing variables at each electrode site. The electric potential Φ is experimentally measured by EEG, not \mathbf{A} , but both are due to the same currents \mathbf{I} . Therefore, \mathbf{A} is linearly proportional to Φ with a simple scaling factor included as a parameter in fits to data. Additional parameterization of background synaptic parameters, B_G^C , and $B_{E'}^{\pm E}$, modify previous work.

The \mathbf{A} model outperformed the no- \mathbf{A} model, where the no- \mathbf{A} model simply has used \mathbf{A} -non-dependent synaptic parameters. Cost functions with an $|\mathbf{A}|$ model were much worse than either the \mathbf{A} model or the no- \mathbf{A} model. Runs with different signs on the drift and on the absolute value of the drift also gave much higher cost functions than the \mathbf{A} model.

3. qPATHINT: Inclusion of Quantum Scales

3.1. SMNI

The wave function ψ_e describing the interaction of \mathbf{A} with \mathbf{p} of Ca^{2+} wave packets was derived in closed form from the Feynman representation of the path integral using path-integral techniques [54].

$$\begin{aligned}\psi_e(t) &= \int d\mathbf{r}_0 \psi_0 \psi_F = \left[\frac{1 - i\hbar t / (m\Delta\mathbf{r}^2)}{1 + i\hbar t / (m\Delta\mathbf{r}^2)} \right]^{1/4} \left[\pi\Delta\mathbf{r}^2 \{1 + [\hbar t / (m\Delta\mathbf{r}^2)]^2\} \right]^{-1/4} \\ &\times \exp \left[-\frac{[\mathbf{r} - (\mathbf{p}_0 + q\mathbf{A})t/m]^2}{2\Delta\mathbf{r}^2} \frac{1 - i\hbar t / (m\Delta\mathbf{r}^2)}{1 + [\hbar t / (m\Delta\mathbf{r}^2)]^2} + i\frac{\mathbf{p}_0 \cdot \mathbf{r}}{\hbar} - i\frac{(\mathbf{p}_0 + q\mathbf{A})^2 t}{2\hbar m} \right] \\ \psi_F(t) &= \int \frac{d\mathbf{p}}{2\pi\hbar} \exp \left[\frac{i}{\hbar} \left(\mathbf{p}(\mathbf{r} - \mathbf{r}_0) - \frac{\mathbf{\Pi}^2 t}{(2m)} \right) \right] = \left[\frac{m}{2\pi i\hbar t} \right]^{1/2} \exp \left[\frac{im(\mathbf{r} - \mathbf{r}_0 - q\mathbf{A}t/m)^2}{2\hbar t} - \frac{i(q\mathbf{A})^2 t}{2m\hbar} \right] \\ \psi_0 &= \psi(\mathbf{r}_0, t = 0) = \left(\frac{1}{\pi\Delta\mathbf{r}^2} \right)^{1/4} \exp \left(-\frac{\mathbf{r}_0^2}{2\Delta\mathbf{r}^2} + i\frac{\mathbf{p}_0 \cdot \mathbf{r}_0}{\hbar} \right)\end{aligned}\quad (9)$$

where ψ_0 is the initial Gaussian packet, ψ_F is the free-wave evolution operator, \hbar is the Planck constant, q is the electronic charge of Ca^{2+} ions, m is the mass of a wave-packet of 1000 Ca^{2+} ions, $\Delta\mathbf{r}^2$ is the spatial variance of the wave-packet, the initial momentum is \mathbf{p}_0 , and the evolving canonical momentum is $\mathbf{\Pi} = \mathbf{p} + q\mathbf{A}$. Detailed calculations show that \mathbf{p} of the Ca^{2+} wave packet and $q\mathbf{A}$ of the EEG field make about equal contributions to $\mathbf{\Pi}$.

3.1.1. SMNI + Ca^{2+} wave-packet

Tripartite influence on synaptic B_G^C , is measured by the ratio of packet's $\langle \mathbf{p}(t) \rangle_{\psi^*\psi}$ to $\langle \mathbf{p}_0(t_0) \rangle_{\psi^*\psi}$ at the onset of each attentional task. Here $\langle \rangle_{\psi^*\psi}$ is taken over $\psi_e^* \psi_e$.

$$\langle \mathbf{p} \rangle_{\psi^*\psi} = m \frac{\langle \mathbf{r} \rangle_{\psi^*\psi}}{t - t_0} = \frac{q\mathbf{A} + \mathbf{p}_0}{m^{1/2}|\Delta\mathbf{r}|} \left(\frac{(\hbar t)^2 + (m\Delta\mathbf{r}^2)^2}{\hbar t + m\Delta\mathbf{r}^2} \right)^{1/2}\quad (10)$$

\mathbf{A} changes slower than \mathbf{p} , so static approximation of \mathbf{A} used to derive ψ_e and $\langle \mathbf{p} \rangle_{\psi^*\psi}$ is reasonable to use within P300 EEG epochs, resetting $t = 0$ at the onset of each classical EEG measurement (1.953 ms apart), using the current \mathbf{A} . This permits tests of interactions across scales in a classical context.

Table 1. Column 1 is the subject number; the other columns are cost functions. Columns 2 and 3 are no-**A** model’s Training (TR0) and Testing (TE0). Columns 4 and 5 are **A** model’s Training (TRA) and Testing (TEA). Columns 6 and 7 are switched no-**A** model’s Training (sTR0) and Testing (sTE0). Columns 8 and 9 are switched **A** model’s Training (sTRA) and Testing (sTEA).

Sub	TR0	TE0	TRA	TEA	sTR0	sTE0	sTRA	sTEA
s01	85.75	121.23	84.76	121.47	120.48	86.59	119.23	87.06
s02	70.80	51.21	68.63	56.51	51.10	70.79	49.36	74.53
s03	61.37	79.81	59.83	78.79	79.20	61.50	75.22	79.17
s04	52.25	64.20	50.09	66.99	63.55	52.83	63.27	64.60
s05	67.28	72.04	66.53	72.78	71.38	67.83	69.60	68.13
s06	84.57	69.72	80.22	64.13	69.09	84.67	61.74	114.21
s07	68.66	78.65	68.28	86.13	78.48	68.73	75.57	69.58
s08	46.58	43.81	44.24	49.38	43.28	47.27	42.89	63.09
s09	47.22	24.88	46.90	25.77	24.68	47.49	24.32	49.94
s10	53.18	33.33	53.33	36.97	33.14	53.85	30.32	55.78
s11	43.98	51.10	43.29	52.76	50.95	44.47	50.25	45.85
s12	45.78	45.14	44.38	46.08	44.92	46.00	44.45	46.56

3.1.2. Results Using $\langle \mathbf{p} \rangle_{\psi^* \psi}$

$\langle \mathbf{p} \rangle_{\psi^* \psi}$ was used in classical-physics SMNI fits to EEG data using ASA. Runs using 1M generated states gave results not much different. Training with ASA used 100K generated states over 12 subjects with and without **A**, followed by 1000 generated states with the simplex local code contained with ASA. Training and Testing runs on XSEDE.org for this project has taken an equivalent of several months of CPU on the XSEDE.org UCSD platform Comet. These calculations use one additional parameter across all EEG regions to weight the contribution to synaptic background $B_{G'}^G$. **A** is taken to be proportional to the currents measured by EEG, i.e., firings M^G . Otherwise, the “zero-fit-parameter” SMNI philosophy was enforced, wherein parameters are picked from experimentally determined values or within experimentally determined ranges [5].

As with previous studies using this data, results sometimes give Testing cost functions less than the Training cost functions. This reflects on great differences in data, likely from great differences in subjects’ contexts, e.g., possibly due to subjects’ STM strategies only sometimes including effects calculated here. Further tests of these multiple-scale models with more EEG data are required, and with the PATHINT-qPATHINT coupled algorithm described in Appendix B.

Table 1 gives recent results on such tests. Cost functions are the effective Action, A_{eff} defined in Appendix B, which is $L \Delta t + \log(\text{prefactor})$, where the prefactor is the normalization of the short-time conditional probability distribution and $L \Delta t$ is the argument of the exponential factor.

3.1.3. Supercomputer Resources

The XSEDE.org University of California San Diego (UCSD) supercomputer resource is Comet.

About 1000 hours of supercomputer CPUs are required for an ASA fit of SMNI to EEG data. Many such sets of runs are required. Including quantum processes will take even longer.

3.2. Quantum Zeno Effects

The quantum-mechanical wave function of the wave packet was shown to “survive” overlaps after multiple collisions, due to their regenerative processes during the observed long durations of hundreds of ms. Thus, Ca^{2+} waves may support a Zeno or “bang-bang” effect which may promote long coherence times [55–62].

Of course, the Zeno/“bang-bang” effect may exist only in special contexts, since decoherence among particles is known to be very fast, e.g., faster than phase-damping of macroscopic classical particles colliding with quantum particles [63].

The wave may be perpetuated by the constant collisions of ions as they enter and leave the wave packet due to the regenerative collisions by the Zeno/“bang-bang” effect. qPATHINT can calculate the coherence stability of the wave due to serial shocks.

3.2.1. Survival of Wave Packet

In momentum space, the wave packet $\phi(\mathbf{p}, t)$ is considered as being “kicked” from \mathbf{p} to $\mathbf{p} + \delta\mathbf{p}$. Assume that random repeated kicks of $\delta\mathbf{p}$ result in $\langle \delta\mathbf{p} \rangle \approx 0$, and that each kick keeps the variance $\Delta(\mathbf{p} + \delta\mathbf{p})^2 \approx \Delta(\mathbf{p})^2$. Then, the overlap integral at the moment t of a typical kick between the new and old state is

$$\begin{aligned} \langle \phi^*(\mathbf{p} + \delta\mathbf{p}, t) | \phi(\mathbf{p}, t) \rangle &= \exp\left(\frac{i\kappa + \rho}{\sigma}\right) \\ \kappa &= 8\delta\mathbf{p}\Delta\mathbf{p}^2\hbar m(q\mathbf{A} + \mathbf{p}_0)t - 4(\delta\mathbf{p}\Delta\mathbf{p}^2t)^2 \\ \rho &= -(\delta\mathbf{p}\hbar m)^2 \\ \sigma &= 8(\Delta\mathbf{p}\hbar m)^2 \end{aligned} \quad (11)$$

where $\phi(\mathbf{p} + \delta\mathbf{p}, t)$ is the normalized wave function in $\mathbf{p} + \delta\mathbf{p}$ momentum space. A crude estimate is obtained of the survival time $A(t)$ and survival probability $p(t)$ [56],

$$\begin{aligned} A(t) &= \langle \phi^*(\mathbf{p} + \delta\mathbf{p}, t) | \phi(\mathbf{p}, t) \rangle \\ p(t) &= |A(t)|^2 \end{aligned} \quad (12)$$

These numbers yield:

$$\langle \phi^*(\mathbf{p} + \delta\mathbf{p}, t) | \phi(\mathbf{p}, t) \rangle = \exp(i(1.67 \times 10^{-1}t - 1.15 \times 10^{-2}t^2) - 1.25 \times 10^{-7}) \quad (13)$$

Even many small repeated kicks do not appreciably affect the real part of ϕ , and these projections do not appreciably destroy the original wave packet, giving a survival probability per kick as $p(t) \approx \exp(-2.5 \times 10^{-7}) \approx 1 - 2.5 \times 10^{-7}$.

The time-dependent phase terms are sensitive to times of tenths of a sec. These times are prominent in STM and in synchronous neural firings. Therefore, \mathbf{A} effects on Ca^{2+} wave functions may maximize their influence on STM at frequencies consistent with synchronous EEG during STM.

All these calculations support this model, in contrast to other models of quantum brain processes without such specific calculations and support [64–66].

4. Applications

This section paraphrases previous papers by this author, including a recent paper [1].

4.1. SMNI

4.1.1. Nano-Robotic Applications

There is the possibility of carrying pharmaceutical products in nanosystems that could affect unbuffered Ca^{2+} waves in neocortex [30]. A Ca^{2+} -wave momentum-sensor could act like a piezoelectric device.

At the onset of a Ca^{2+} wave (on the order of 100's of ms), a change of momentum can be on the order of 10^{-30} kg-m/s for a typical Ca^{2+} ion. A Ca^{2+} wave packet of 1000 ions with onset time of 1 ms,

exerts a force on the order of 10^{-24} N ($1 \text{ N} \equiv 1 \text{ Newton} = 1 \text{ kg}\cdot\text{m}/\text{s}^2$). A nano-robot would be attracted to this site, depositing chemicals/drugs that interact with the regenerative Ca^{2+} -wave process.

An area of the receptor of the nanosystem of 1 nm^2 would require pressure sensitivity of 10^{-6} Pa ($1 \text{ Pa} = 1 \text{ pascal} = 1 \text{ N}/\text{m}^2$).

The nano-robot could be switched on/off at a regional/columnar level by sensitivity to local electric/magnetic fields. Highly synchronous firings during STM processes can be affected by these piezoelectric nanosystems which affect background/noise efficacies via control of Ca^{2+} waves. In turn, this would affect the influence of Ca^{2+} waves via the vector potential \mathbf{A} , etc.

4.1.2. Free Will

There is interest in researching possible quantum influences on highly synchronous neuronal firings relevant to STM to understand connections to consciousness and “Free Will” (FW) [31,67].

If experimental evidence is gained of quantum-level processes of tripartite synaptic interactions with large-scale synchronous neuronal firings, then FW may be established using the Conway-Kochen quantum no-clone “Free Will Theorem” (FWT) [68,69].

Since quantum states cannot be cloned, a Ca^{2+} quantum wave-packet may not generate a state proven to have previously existed;

5. Conclusion

The SMNI model has demonstrated it is faithful to experimental data, for EEG recordings under STM experimental paradigms. qPATHINT permits an inclusion of quantum scales in the multiple-scale SMNI model, by evolving Ca^{2+} wave-packets with momentum \mathbf{p} , including serial shocks, interacting with the magnetic vector potential \mathbf{A} derived from EEG data, marching forward in time lock-step with experimental EEG data. This presents a time-dependent propagation of interacting quantum and classical scales.

This quantum path-integral algorithm with serial random shocks will be further studied as it can be used for many quantum systems.

Appendix A. Adaptive Simulated Annealing (ASA) Algorithm

This section paraphrases previous papers by this author, including a recent paper [1].

Appendix A.1 Importance Sampling

Nonlinear and/or stochastic systems often require importance-sampling algorithms to scan or to fit parameters. Methods of simulated annealing (SA) are often used. Proper annealing (not “quenching”) possesses a proof of finding the deepest minimum in searches.

The ASA code is open-source software, and can be downloaded and used without any cost or registration at <https://www.ingber.com/#ASA> [20,21].

This algorithm fits empirical data to a cost function over a D -dimensional parameter space, adapting for varying sensitivities of parameters during the fit.

This ASA algorithm is faster than fast Cauchy annealing, which has schedule $T_i = T_0/k$, and much faster than Boltzmann annealing, which has schedule $T_i = T_0/\ln k$ [19].

Appendix A.2 Outline of ASA Algorithm

For parameters

$$\alpha_k^i \in [A_i, B_i]$$

sampling with the random variable x^i

$$x^i \in [-1, 1]$$

$$\alpha_{k+1}^i = \alpha_k^i + x^i(B_i - A_i)$$

the default generating function is

$$g_T(x) = \prod_{i=1}^D \frac{1}{2 \ln(1 + 1/T_i)(|x^i| + T_i)} \equiv \prod_{i=1}^D g_T^i(x^i)$$

in terms of parameter “temperatures”

$$T_i = T_{i0} \exp(-c_i k^{1/D}) \quad (\text{A1})$$

The default ASA uses the same type of annealing schedule for the acceptance function h as used for the generating function g .

All default functions in ASA can be overridden with user-defined functions.

Appendix A.3 Applications

The ASA code [20] and the original Very Fast Simulated Reannealing (VFSR) code [19] have been used by many researchers, including the author in a range of disciplines:

chaotic systems [70]
 combat simulations [71,72]
 financial systems: bonds, equities, futures, options [73–78]
 neuroscience [8,14,29,30,33,34,39,70,79–87]
 optimization *per se* [19,21–23,88,89]

Appendix B. Path-Integral Algorithms PATHINT and qPATHINT

This section paraphrases previous papers by this author, including a recent paper [1].

Appendix B.1 Path Integral in Stratonovich (Midpoint) Representation

The path integral in the Feynman (midpoint) representation is used to examine discretization issues in time-dependent nonlinear systems [90–92]. (N.b. g^\dagger in DM implies a prepoint evaluation.) Unless explicitly stated, the Einstein summation convention is used which implies repeated indices signify summation; bars $|\dots|$ imply no summation.

$$P[M_t|M_{t_0}]dM(t) = \int \dots \int DM \exp\left(-\min \int_{t_0}^t dt' L\right) \delta(M(t_0) = M_0) \delta(M(t) = M_t)$$

$$DM = \lim_{u \rightarrow \infty} \prod_{\rho=1}^{u+1} g^{+1/2} \prod_G (2\pi\theta)^{-1/2} dM_\rho^G$$

$$L(\dot{M}^G, M^G, t) = \frac{1}{2}(\dot{M}^G - h^G)g_{GG'}(\dot{M}^{G'} - h^{G'}) + \frac{1}{2}h_{;G}^G + R/6 - V$$

$$\dot{M}^G(t) \rightarrow M_{\rho+1}^G - M_\rho^G, M^G(t) \rightarrow \frac{1}{2}(M_{\rho+1}^G + M_\rho^G), [\dots]_{,G} = \frac{\partial[\dots]}{\partial M^G}$$

$$h^G = g^G - \frac{1}{2}g^{-1/2}(g^{1/2}g^{GG'})_{,G'}, h_{;G}^G = h_{,G}^G + \Gamma_{GF}^F h^G = g^{-1/2}(g^{1/2}h^G)_{,G}$$

$$g_{GG'} = (g^{GG'})^{-1}, g = \det(g_{GG'})$$

$$\Gamma_{JK}^F \equiv g^{LF}[JK, L] = g^{LF}(g_{JL,K} + g_{KL,I} - g_{JK,L})$$

$$R = g^{JL}R_{JL} = g^{JL}g^{JK}R_{FJKL}$$

$$R_{FJKL} = \frac{1}{2}(g_{FK,JL} - g_{JK,FL} - g_{FL,JK} + g_{JL,FK}) + g_{MN}(\Gamma_{FK}^M \Gamma_{JL}^N - \Gamma_{FL}^M \Gamma_{JK}^N) \quad (\text{A2})$$

Non-constant diffusions add terms to drifts, and a Riemannian-curvature potential $R/6$ is induced for dimension > 1 in the Stratonovich/Feynman discretization.

Appendix B.2 Path Integral in Ito (Prepoint) Representation

In the Ito (prepoint) representation:

$$P[M_t|M_{t_0}]dM(t) = \int \dots \int DM \exp\left(-\min_{t_0}^t \int dt' L\right) \delta(M(t_0) = M_0) \delta(M(t) = M_t)$$

$$DM = \lim_{u \rightarrow \infty} \prod_{\rho=1}^{u+1} g^{1/2} \prod_G (2\pi\Delta t)^{-1/2} dM_\rho^G$$

$$L(\dot{M}^G, M^G, t) = \frac{1}{2}(\dot{M}^G - g^G)g_{GG'}(\dot{M}^{G'} - g^{G'}) + R/6$$

$$\dot{M}^G(t) \rightarrow M_{\rho+1}^G - M_\rho^G, M^G(t) \rightarrow M_\rho^G$$

$$g_{GG'} = (g^{GG'})^{-1}, g = \det(g_{GG'}) \quad (\text{A3})$$

Here the diagonal diffusions are $g^{|GG|}$ and the drifts are g^G .

Appendix B.3 Path-Integral Riemannian Geometry

The midpoint derivation derives a Riemannian geometry with metric defined by the inverse of the covariance matrix

$$g_{GG'} = (g^{GG'})^{-1} \quad (\text{A4})$$

and where R is the Riemannian curvature

$$R = g^{JL}R_{JL} = g^{JL}g^{JK}R_{FJKL} \quad (\text{A5})$$

An Ito prepoint discretization for the same probability distribution P gives a simpler algebraic form,

$$M(\bar{t}_s) = M(t_s)$$

$$L = \frac{1}{2}(dM^G/dt - g^G)g_{GG'}(dM^{G'}/dt - g^{G'}) - V \quad (\text{A6})$$

but the Lagrangian L so specified does not satisfy a variational principle useful for moderate to large noise. Its variational principle is only useful in the weak-noise limit. This often means that finer meshes are required.

Appendix B.4 Three Approaches Are Mathematically Equivalent

Three basic different approaches are mathematically equivalent:

- (a) Fokker-Planck/Chapman-Kolmogorov partial-differential equations
- (b) Langevin coupled stochastic-differential equations
- (c) Lagrangian or Hamiltonian path-integrals

The path-integral approach is useful to define intuitive physical variables from the Lagrangian L in terms of underlying variables M^G :

$$\begin{aligned}
 \text{Momentum : } \Pi^G &= \frac{\partial L}{\partial(\partial M^G / \partial t)} \\
 \text{Mass : } g_{GG'} &= \frac{\partial L}{\partial(\partial M^G / \partial t) \partial(\partial M^{G'} / \partial t)} \\
 \text{Force : } &\frac{\partial L}{\partial M^G} \\
 F = ma : \delta L = 0 &= \frac{\partial L}{\partial M^G} - \frac{\partial}{\partial t} \frac{\partial L}{\partial(\partial M^G / \partial t)} \tag{A7}
 \end{aligned}$$

Differentiation especially of noisy systems often introduces more noise. The path-integral often gives superior numerical performance because integration is a smoothing process.

Appendix B.5 Stochastic Differential Equation (SDE)

The Stratonovich (midpoint discretized) Langevin equations can be analyzed in terms of the Wiener process dW^i . This can be developed with Gaussian noise $\eta^i = dW^i / dt$, with some care taken in the limit of small dt .

$$dM^G = f^G(t, M(t))dt + \hat{g}_i^G(t, M(t))dW^i$$

$$\dot{M}^G(t) = f^G(t, M(t)) + \hat{g}_i^G(t, M(t))\eta^i(t)$$

$$dW^i \rightarrow \eta^i dt$$

$$M = \{M^G; G = 1, \dots, \Lambda\}$$

$$\eta = \{\eta^i; i = 1, \dots, N\}$$

$$\dot{M}^G = dM^G / dt$$

$$\langle \eta^j(t) \rangle_{\eta} = 0, \langle \eta^j(t), \eta^{j'}(t') \rangle_{\eta} = \delta^{jj'} \delta(t - t') \tag{A8}$$

η^i represents Gaussian white noise.

Appendix B.6 Partial Differential Equation (PDE)

The Fokker-Planck, sometimes defines as Chapman-Kolmogorov, partial differential equation is:

$$P_{,t} = \frac{1}{2}(g^{GG'} P)_{,GG'} - (g^G P)_{,G} + VP$$

$$\begin{aligned}
P &= \langle P_\eta \rangle_\eta \\
g^G &= f^G + \frac{1}{2} \hat{g}_i^{G'} \hat{g}_{i,G}^G \\
g^{GG'} &= \hat{g}_i^G \hat{g}_i^{G'} \\
(\dots)_{,G} &= \partial(\dots) / \partial M^G
\end{aligned} \tag{A9}$$

g^G replaces f^G in the SDE if the Ito (prepoint discretized) calculus is used. If boundary conditions are added as Lagrange multipliers, these enter as a “potential” V creating a Schrodinger-type equation.

Appendix B.7 Applications

Path integrals and PATHINT have been applied across several disciplines, including combat simulations [93], neuroscience [1,7,39,87], finance [1,32,67,75,77,94,95], and other nonlinear systems [70,72,96].

Appendix B.8 PATHINT/qPATHINT Code

qPATHINT is an N-dimensional code developed to calculate the propagation of quantum variables in the presence of shocks. Many real systems propagate in the presence of sudden changes of state dependent on time. qPATHINT is based on the classical-physics code, PATHINT, which has been useful in several systems across several disciplines. Applications have been made to Statistical Mechanics of Neocortical Interactions (SMFI) and Statistical Mechanics of Financial Markets (SMFM) [1,32,94].

To numerically calculate the path integral for serial changes in time, standard Monte Carlo techniques generally are not useful. PATHINT was originally developed for this purpose. The PATHINT C code of about 7500 lines of code using the GCC C-compiler was rewritten to use double complex variables instead of double variables, and further developed for arbitrary N dimensions, creating qPATHINT. The outline of the code is described here for classical or quantum systems, using generic coordinates q and x [32,67,94]:

The distribution (probabilities for classical systems, wave-functions for quantum systems) can be numerically approximated to a high degree of accuracy using a histogram procedure, developing sums of rectangles of height P_i and width Δq^i at points q^i .

Appendix B.8.1 Shocks

Many real-world systems propagate in the presence of continual “shocks”.

In SMNI, collisions occur via regenerative Ca^{2+} waves. There also are interactions with changing \mathbf{A} due to changing highly synchronous neuronal firings.

In SMFM applications, shocks occur due to future dividends, changes in interest rates, changes in asset distributions, etc.

Appendix B.8.2 PATHINT/qPATHINT Histograms

A one-dimensional path-integral in variable x in the prepoint Ito discretization is developed in terms of the kernel G , for each of its intermediate integrals, as

$$P(x; t + \Delta t) = \int dx' [g^{1/2} (2\pi\Delta t)^{-1/2} \exp(-L\Delta t)] P(x'; t) = \int dx' G(x, x'; \Delta t) P(x'; t)$$

$$P(x; t) = \sum_{i=1}^N \pi(x - x^i) P_i(t)$$

$$\pi(x - x^i) = 1, (x^i - \frac{1}{2}\Delta x^{i-1}) \leq x \leq (x^i + \frac{1}{2}\Delta x^i); 0, \text{ otherwise} \quad (\text{A10})$$

This yields

$$P_i(t + \Delta t) = T_{ij}(\Delta t) P_j(t)$$

$$T_{ij}(\Delta t) = \frac{2}{\Delta x^{i-1} + \Delta x^i} \int_{x^i - \Delta x^{i-1}/2}^{x^i + \Delta x^i/2} dx \int_{x^j - \Delta x^{j-1}/2}^{x^j + \Delta x^j/2} dx' G(x, x'; \Delta t) \quad (\text{A11})$$

T_{ij} is a banded matrix representing the Gaussian nature of the short-time probability centered about the drift.

Several projects have used this algorithm [39,70,97–100]. Special 2-dimensional codes were developed for specific projects in Statistical Mechanics of Combat (SMC), SMNI and SMFM [39,75,93].

Appendix B.8.3 Meshes For [q]PATHINT

Explicit dependence of L on time t can be included. The mesh Δq^i is strongly dependent on diagonal elements of the diffusion matrix, e.g.,

$$\Delta q^i \approx (\Delta t g^{i|i})^{1/2} \quad (\text{A12})$$

This constrains the dependence of the covariance of each variable to be a (nonlinear) function of that variable to present a rectangular underlying mesh. Since integration is inherently a smoothing process [73], coarser meshes are used relative to the corresponding stochastic differential equation(s) [98].

By considering the contributions to the first and second moments, conditions on the time and variable meshes can be derived. Thus Δt can be measured by the diffusion divided by the square of the drift.

Appendix B.9 Lessons Learned From SMFM and SMNI

SMNI qPATHINT has emphasized the requirement of broad-banded kernels for oscillatory quantum states.

SMFM PATHTREE, and its derived qPATHTREE, is a different options code, based on path-integral error analyses, permitting a new very fast binary calculation, also applied to nonlinear time-dependent systems [77]. However, in contrast to the present PATHINT/qPATHINT code that has been generalized to N dimensions, currently an SMFM [q]PATHTREE is only a binary tree with $J = 1$ and cannot be effectively applied to quantum oscillatory systems [32,67,94].

Appendix B.9.1 Calculations At Each Node At Each Time Slice

SMFM (q)PATHINT for (American) financial options: Calculate at each node of each time slice — back in time.

SMNI (q)PATHINT: Calculate at each node of each time slice — forward in time.

At each node of each time slice, a proposed algorithm is to calculate quantum-scale Ca^{2+} wave-packet (2-way) interactions with macroscopic large-scale EEG/A. This entails algorithms:

PATHINT using the Classical SMNI Lagrangian

qPATHINT using the Quantum Ca^{2+} wave-packet Lagrangian

Sync in time during P300 attentional tasks.

Time/phase relations between classical and quantum systems may be important.

ASA-fit synchronized classical-quantum PATHINT-qPATHINT model to EEG data.

$\mathbf{A}(\text{EEG})$ is determined experimentally, and includes all synaptic background $B_{C'}^G$ effects.

\$Id: https://www.ingber.com/smni18_quantumCaEEG.pdf 1.20 2018/08/14 20:48:56 ingber Exp
ingber\$

1. Ingber, L. Quantum Path-Integral qPATHINT Algorithm. *The Open Cybernetics Systemics Journal* **2017a**, *11*, 119–133. <http://dx.doi.org/10.2174/1874110X01711010119>.
2. Ingber, L. Towards a unified brain theory. *Journal Social Biological Structures* **1981**, *4*, 211–224. https://www.ingber.com/smni81_unified.pdf.
3. Ingber, L. Statistical mechanics of neocortical interactions. I. Basic formulation. *Physica D* **1982**, *5*, 83–107. https://www.ingber.com/smni82_basic.pdf.
4. Ingber, L. Statistical mechanics of neocortical interactions. Dynamics of synaptic modification. *Physical Review A* **1983**, *28*, 395–416. https://www.ingber.com/smni83_dynamics.pdf.
5. Ingber, L. Statistical mechanics of neocortical interactions. Derivation of short-term-memory capacity. *Physical Review A* **1984**, *29*, 3346–3358. https://www.ingber.com/smni84_stm.pdf.
6. Ingber, L. Statistical mechanics of neocortical interactions: Stability and duration of the 7+2 rule of short-term-memory capacity. *Physical Review A* **1985a**, *31*, 1183–1186. https://www.ingber.com/smni85_stm.pdf.
7. Ingber, L. Statistical mechanics of neocortical interactions: Path-integral evolution of short-term memory. *Physical Review E* **1994**, *49*, 4652–4664. https://www.ingber.com/smni94_stm.pdf.
8. Ingber, L. Columnar EEG magnetic influences on molecular development of short-term memory. In *Short-Term Memory: New Research*; Kalivas, G.; Petralia, S., Eds.; Nova: Hauppauge, NY, 2012a; pp. 37–72. Invited Paper. https://www.ingber.com/smni11_stm_scales.pdf.
9. Ericsson, K.; Chase, W. Exceptional memory. *American Scientist* **1982**, *70*, 607–615.
10. Zhang, G.; Simon, H. STM capacity for Chinese words and idioms: Chunking and acoustical loop hypotheses. *Memory & Cognition* **1985**, *13*, 193–201.
11. Hick, W. On the rate of gains of information. *Quarterly Journal Experimental Psychology* **1952**, *34*, 1–33.
12. Ingber, L. Statistical mechanics of neocortical interactions: Reaction time correlates of the g factor. *Psychology* **1999**, *10*. Invited commentary on The g Factor: The Science of Mental Ability by Arthur Jensen. https://www.ingber.com/smni99_g_factor.pdf.
13. Jensen, A. Individual differences in the Hick paradigm. In *Speed of Information-Processing and Intelligence*; Vernon, P., Ed.; Ablex: Norwood, NJ, 1987; pp. 101–175.
14. Ingber, L. Statistical mechanics of neocortical interactions: Applications of canonical momenta indicators to electroencephalography. *Physical Review E* **1997a**, *55*, 4578–4593. https://www.ingber.com/smni97_cmi.pdf.
15. Ingber, L. *EEG Database*; UCI Machine Learning Repository: Irvine, CA, 1997b. <http://archive.ics.uci.edu/ml/datasets/EEG+Database>.
16. Ingber, L. Ideas by statistical mechanics (ISM). Technical Report Report 2006:ISM, Lester Ingber Research, Ashland, OR, 2006a. https://www.ingber.com/smni06_ism.pdf.
17. Ingber, L. Ideas by Statistical Mechanics (ISM). *Journal Integrated Systems Design and Process Science* **2007**, *11*, 31–54. Special Issue: Biologically Inspired Computing.
18. Ingber, L. AI and Ideas by Statistical Mechanics (ISM). In *Encyclopedia of Artificial Intelligence*; Rabunal, J.; Dorado, J.; Pazos, A., Eds.; Information Science Reference: New York, 2008; pp. 58–64. ISBN 978-1-59904-849-9.
19. Ingber, L. Very fast simulated re-annealing. *Mathematical Computer Modelling* **1989**, *12*, 967–973. https://www.ingber.com/asa89_vfsr.pdf.
20. Ingber, L. Adaptive Simulated Annealing (ASA). Technical Report Global optimization C-code, Caltech Alumni Association, Pasadena, CA, 1993a. <https://www.ingber.com/#ASA-CODE>.
21. Ingber, L. Adaptive Simulated Annealing. In *Stochastic global optimization and its applications with fuzzy adaptive simulated annealing*; H.A. Oliveira, J.; Petraglia, A.; Ingber, L.; Machado, M.; Petraglia, M., Eds.; Springer: New York, 2012b; pp. 33–61. Invited Paper. https://www.ingber.com/asa11_options.pdf.
22. Ingber, L. Simulated annealing: Practice versus theory. *Mathematical Computer Modelling* **1993b**, *18*, 29–57. https://www.ingber.com/asa93_sapvt.pdf.

23. Atiya, A.; Parlos, A.; Ingber, L. A reinforcement learning method based on adaptive simulated annealing. In *Proceedings International Midwest Symposium on Circuits and Systems (MWCAS), December 2003*; IEEE CAS: Cairo, Egypt, 2003. https://www.ingber.com/asa03_reinforce.pdf.
24. Ingber, L. Statistical mechanics of multiple scales of neocortical interactions. In *Neocortical Dynamics and Human EEG Rhythms*; Nunez, P., Ed.; Oxford University Press: New York, NY, 1995a; pp. 628–681. ISBN 0-19-505728-7. https://www.ingber.com/smni95_scales.pdf.
25. Asher, J. Brain's code for visual working memory deciphered in monkeys NIH-funded study. Technical Report NIH Press Release, NIH, Bethesda, MD, 2012. <http://www.nimh.nih.gov/news/science-news/2012/in-sync-brain-waves-hold-memory-of-objects-just-seen.shtml>.
26. Salazar, R.; Dotson, N.; Bressler, S.; Gray, C. Content-specific fronto-parietal synchronization during visual working memory. *Science* **2012**, *338*, 1097–1100. <http://dx.doi.org/10.1126/science.1224000>.
27. Ingber, L. Statistical mechanics of neocortical interactions: Constraints on 40 Hz models of short-term memory. *Physical Review E* **1995b**, *52*, 4561–4563. https://www.ingber.com/smni95_stm40hz.pdf.
28. Ingber, L. Computational algorithms derived from multiple scales of neocortical processing. In *Pointing at Boundaries: Integrating Computation and Cognition on Biological Grounds*; A. Pereira, J.; Massad, E.; Bobbitt, N., Eds.; Springer: New York, 2011; pp. 1–13. Invited Paper. <http://dx.doi.org/10.1007/s12559-011-9105-4>.
29. Ingber, L. Influence of macrocolumnar EEG on Ca waves. *Current Progress Journal* **2012c**, *1*, 4–8. https://www.ingber.com/smni12_vectpot.pdf.
30. Ingber, L. Calculating consciousness correlates at multiple scales of neocortical interactions. In *Horizons in Neuroscience Research*; Costa, A.; Villalba, E., Eds.; Nova: Hauppauge, NY, 2015; pp. 153–186. ISBN: 978-1-63482-632-7. Invited paper. https://www.ingber.com/smni15_calc_conscious.pdf.
31. Ingber, L. Statistical mechanics of neocortical interactions: Large-scale EEG influences on molecular processes. *Journal of Theoretical Biology* **2016a**, *395*, 144–152. <http://dx.doi.org/10.1016/j.jtbi.2016.02.003>.
32. Ingber, L. Evolution of regenerative Ca-ion wave-packet in neuronal-firing fields: Quantum path-integral with serial shocks. *International Journal of Innovative Research in Information Security* **2017b**, *4*, 14–22. https://www.ingber.com/path17_quantum_pathint_shocks.pdf.
33. Ingber, L.; Pappalepore, M.; Stesiak, R. Electroencephalographic field influence on calcium momentum waves. *Journal of Theoretical Biology* **2014**, *343*, 138–153. <http://dx.doi.org/10.1016/j.jtbi.2013.11.002>.
34. Nunez, P.; Srinivasan, R.; Ingber, L. Theoretical and experimental electrophysiology in human neocortex: Multiscale correlates of conscious experience. In *Multiscale Analysis and Nonlinear Dynamics: From genes to the brain*; Pesenson, M., Ed.; Wiley: New York, 2013; pp. 149–178. <http://dx.doi.org/10.1002/9783527671632.ch06>.
35. Ingber, L. Towards clinical applications of statistical mechanics of neocortical interactions. *Innovations Technology Biology Medicine* **1985b**, *6*, 753–758.
36. Ingber, L. Statistical mechanics of neocortical interactions. EEG dispersion relations. *IEEE Transactions in Biomedical Engineering* **1985c**, *32*, 91–94. https://www.ingber.com/smni85_eeg.pdf.
37. Briggs, F.; Mangun, G.; Usrey, W. Attention enhances synaptic efficacy and the signal-to-noise ratio in neural circuits. *Nature* **2013**, *000*, 1–5. <http://dx.doi.org/10.1038/nature12276>.
38. Mountcastle, V.; Andersen, R.; Motter, B. The influence of attentive fixation upon the excitability of the light-sensitive neurons of the posterior parietal cortex. *Journal of Neuroscience* **1981**, *1*, 1218–1235.
39. Ingber, L.; Nunez, P. Statistical mechanics of neocortical interactions: High resolution path-integral calculation of short-term memory. *Physical Review E* **1995**, *51*, 5074–5083. https://www.ingber.com/smni95_stm.pdf.
40. Agulhon, C.; Petravicz, J.; McMullen, A.; Sweger, E.; Minton, S.; Taves, S.; Casper, K.; Fiacco, T.; McCarthy, K. What is the role of astrocyte calcium in neurophysiology? *Neuron* **2008**, *59*, 932–946.
41. Araque, A.; Navarrete, M. Glial cells in neuronal network function. *Philosophical Transactions of The Royal Society B* **2010**, pp. 2375–2381.
42. Banaclocha, M.; Bookkon, I.; Banaclocha, H. Long-term memory in brain magnetite. *Medical Hypotheses* **2010**, *74*, 254–257.
43. Bellingier, S. Modeling calcium wave oscillations in astrocytes. *Neurocomputing* **2005**, *65*, 843–850.
44. Innocenti, B.; Parpura, V.; Haydon, P. Imaging extracellular waves of glutamate during calcium signaling in cultured astrocytes. *Journal of Neuroscience* **2000**, *20*, 1800–1808.

45. A. Pereira, J.; Furlan, F. On the role of synchrony for neuron-astrocyte interactions and perceptual conscious processing. *Journal of Biological Physics* **2009**, *35*, 465–480.
46. Reyes, R.; Parpura, V. The trinity of Ca²⁺ sources for the exocytotic glutamate release from astrocytes. *Neurochemistry International* **2009**, *55*, 1–14.
47. Scemes, E.; Giaume, C. Astrocyte calcium waves: What they are and what they do. *Glia* **2006**, *54*, 716–725. <http://dx.doi.org/10.1002/glia.20374>.
48. Voltterra, A.; Liaudet, N.; Savtchouk, I. Astrocyte Ca²⁺ signalling: an unexpected complexity. *Nature Reviews Neuroscience* **2014**, *15*, 327–335.
49. Ross, W. Understanding calcium waves and sparks in central neurons. *Nature Reviews Neuroscience* **2012**, *13*, 157–168.
50. Murakami, S.; Okada, Y. Contributions of principal neocortical neurons to magnetoencephalography and electroencephalography signals. *Journal of Physiology* **2006**, *575*, 925–936.
51. Nunez, P.; Srinivasan, R. *Electric Fields of the Brain: The Neurophysics of EEG, 2nd Ed*; Oxford University Press: London, 2006.
52. Citi, L.; Poli, R.; Cinel, C. Documenting, modelling and exploiting P300 amplitude changes due to variable target delays in Donchin's speller. *Journal of Neural Engineering* **2010**, *7*, 1–21. <http://dx.doi.org/10.1088/1741-2560/7/5/056006>.
53. Goldberger, A.; Amaral, L.; Glass, L.; Hausdorff, J.; Ivanov, P.; Mark, R.; Mietus, J.; Moody, G.; Peng, C.K.; Stanley, H. PhysioBank, PhysioToolkit, and PhysioNet: Components of a New Research Resource for Complex Physiologic Signals. *Circulation* **2000**, *101*, e215–e220. <http://circ.ahajournals.org/cgi/content/full/101/23/e215>.
54. Schulten, K. Quantum Mechanics. Technical Report Lecture Notes, U. Illinois, Urbana, IL, 1999. <http://www.ks.uiuc.edu/Services/Class/PHYS480/>.
55. Facchi, P.; Lidar, D.; Pascazio, S. Unification of dynamical decoupling and the quantum Zeno effect. *Physical Review A* **2004**, *69*, 1–6.
56. Facchi, P.; Pascazio, S. Quantum Zeno dynamics: mathematical and physical aspects. *Journal of Physics A* **2008**, *41*, 1–45.
57. Giacosa, G.; Pagliara, G. Quantum Zeno effect by general measurements. *Physical Review A* **2014**, *052107*, 1–5.
58. Kozłowski, W.; Caballero-Benitez, S.; Mekhov, I. Non-Hermitian dynamics in the quantum Zeno limit. Technical Report arXiv:1510.04857 [quant-ph], U Oxford, Oxford, UK, 2015.
59. Muller, M.; Gherardini, S.; Caruso, F. Quantum Zeno Dynamics through stochastic protocols. Technical Report arXiv:1607.08871v1 [quant-ph], U Florence, Florence, Italy, 2016.
60. Patil, Y.; Chakram, S.; Vengalattore, M. Measurement-induced localization of an ultracold lattice gas. *Physical Review Letters* **2015**, *115*, 1–5. <http://link.aps.org/doi/10.1103/PhysRevLett.115.140402>.
61. Wu, S.; Wang, L.; Yi, X. Time-dependent decoherence-free subspace. *Journal of Physics A* **2012**, *405305*, 1–11.
62. Zhang, P.; Ai, Q.; Li, Y.; Xu, D.; Sun, C. Dynamics of quantum Zeno and anti-Zeno effects in an open system. *Science China Physics, Mechanics & Astronomy* **2014**, *57*, 194–207. <http://dx.doi.org/10.1007/s11433-013-5377-x>.
63. Preskill, J. Quantum Mechanics. Technical Report Lecture Notes, Caltech, Pasadena, CA, 2015. <http://www.theory.caltech.edu/people/preskill/ph219/>.
64. Hagan, S.; Hameroff, S.; Tuszynski, J. Quantum computation in brain microtubules: Decoherence and biological feasibility. *Physical Review E* **2002**, *65*, 1–11. <http://link.aps.org/doi/10.1103/PhysRevE.65.061901>.
65. Hameroff, S.; Penrose, R. Consciousness in the universe: A review of the 'Orch OR' theory. *Physics of Life Reviews* **2013**, *403*, 1–40. <http://dx.doi.org/10.1016/j.plrev.2013.08.002>.
66. McKemmish, L.; Reimers, J.; McKenzie, R.; Mark, A.; Hush, N. Penrose-Hameroff orchestrated objective-reduction proposal for human consciousness is not biologically feasible. *Physical Review E* **2009**, *80*, 1–6. <http://link.aps.org/doi/10.1103/PhysRevE.80.021912>.
67. Ingber, L. Path-integral quantum PATHTREE and PATHINT algorithms. *International Journal of Innovative Research in Information Security* **2016b**, *3*, 1–15. https://www.ingber.com/path16_quantum_path.pdf.
68. Conway, J.; Kochen, S. The free will theorem. Technical Report arXiv:quant-ph/0604079 [quant-ph], Princeton U, Princeton, NJ, 2006.

69. Conway, J.; Kochen, S. The strong free will theorem. *Notices of the American Mathematical Society* **2009**, *56*, 226–232.
70. Ingber, L.; Srinivasan, R.; Nunez, P. Path-integral evolution of chaos embedded in noise: Duffing neocortical analog. *Mathematical Computer Modelling* **1996**, *23*, 43–53. https://www.ingber.com/path96_duffing.pdf.
71. Ingber, L. Statistical mechanics of combat and extensions. In *Toward a Science of Command, Control, and Communications*; Jones, C., Ed.; American Institute of Aeronautics and Astronautics: Washington, D.C., 1993c; pp. 117–149. ISBN 1-56347-068-3. https://www.ingber.com/combat93_c3sci.pdf.
72. Ingber, L. Data mining and knowledge discovery via statistical mechanics in nonlinear stochastic systems. *Mathematical Computer Modelling* **1998a**, *27*, 9–31. https://www.ingber.com/path98_datamining.pdf.
73. Ingber, L. Statistical mechanical aids to calculating term structure models. *Physical Review A* **1990**, *42*, 7057–7064. https://www.ingber.com/markets90_interest.pdf.
74. Ingber, L. Canonical momenta indicators of financial markets and neocortical EEG. In *Progress in Neural Information Processing*; Amari, S.I.; Xu, L.; King, I.; Leung, K.S., Eds.; Springer: New York, 1996a; pp. 777–784. Invited paper to the 1996 International Conference on Neural Information Processing (ICONIP'96), Hong Kong, 24–27 September 1996. ISBN 981-3083-05-0. https://www.ingber.com/markets96_momenta.pdf.
75. Ingber, L. High-resolution path-integral development of financial options. *Physica A* **2000**, *283*, 529–558. https://www.ingber.com/markets00_highres.pdf.
76. Ingber, L. Trading in Risk Dimensions (TRD). Technical Report Report 2005:TRD, Lester Ingber Research, Ashland, OR, 2005. https://www.ingber.com/markets05_trd.pdf.
77. Ingber, L.; Chen, C.; Mondescu, R.; Muzzall, D.; Renedo, M. Probability tree algorithm for general diffusion processes. *Physical Review E* **2001**, *64*, 056702–056707. https://www.ingber.com/path01_pathtree.pdf.
78. Ingber, L.; Mondescu, R. Automated internet trading based on optimized physics models of markets. In *Intelligent Internet-Based Information Processing Systems*; Howlett, R.; Ichalkaranje, N.; Jain, L.; Tonfoni, G., Eds.; World Scientific: Singapore, 2003; pp. 305–356. Invited paper. https://www.ingber.com/markets03_automated.pdf.
79. Ingber, L. Statistical mechanics of neocortical interactions: A scaling paradigm applied to electroencephalography. *Physical Review A* **1991**, *44*, 4017–4060. https://www.ingber.com/smni91_eeg.pdf.
80. Ingber, L. Generic mesoscopic neural networks based on statistical mechanics of neocortical interactions. *Physical Review A* **1992**, *45*, R2183–R2186. https://www.ingber.com/smni92_mnn.pdf.
81. Ingber, L. Statistical mechanics of neocortical interactions: Multiple scales of EEG. In *Frontier Science in EEG: Continuous Waveform Analysis (Electroencephal. clin. Neurophysiol. Suppl. 45)*; Dasheiff, R.; Vincent, D., Eds.; Elsevier: Amsterdam, 1996b; pp. 79–112. Invited talk to Frontier Science in EEG Symposium, New Orleans, 9 Oct 1993. ISBN 0-444-82429-4. https://www.ingber.com/smni96_eeg.pdf.
82. Ingber, L. Statistical mechanics of neocortical interactions: Training and testing canonical momenta indicators of EEG. *Mathematical Computer Modelling* **1998b**, *27*, 33–64. https://www.ingber.com/smni98_cmi_test.pdf.
83. Ingber, L. Statistical mechanics of neocortical interactions: Portfolio of physiological indicators. Technical Report Report 2006:PPI, Lester Ingber Research, Ashland, OR, 2006b. https://www.ingber.com/smni06_ppi.pdf.
84. Ingber, L. Statistical mechanics of neocortical interactions: Portfolio of physiological indicators. *The Open Cybernetics Systemics Journal* **2009a**, *3*, 13–26. <http://dx.doi.org/10.2174/1874110x00903010013>.
85. Ingber, L. Statistical mechanics of neocortical interactions: Nonlinear columnar electroencephalography. *NeuroQuantology Journal* **2009b**, *7*, 500–529. https://www.ingber.com/smni09_nonlin_column_eeg.pdf.
86. Ingber, L. Electroencephalographic (EEG) influence on Ca²⁺ waves: Lecture plates. Technical Report Report 2013:LEFI, Lester Ingber Research, Ashland, OR, 2013. 2nd World Neuroscience Online Conference 18 June 2013. https://www.ingber.com/smni13_eeg_ca_lect.pdf.
87. Ingber, L.; Nunez, P. Neocortical Dynamics at Multiple Scales: EEG Standing Waves, Statistical Mechanics, and Physical Analogs. *Mathematical Biosciences* **2010**, *229*, 160–173. https://www.ingber.com/smni10_multiple_scales.pdf.
88. Ingber, L. Adaptive simulated annealing (ASA): Lessons learned. *Control and Cybernetics* **1996c**, *25*, 33–54. Invited paper to Control and Cybernetics on Simulated Annealing Applied to Combinatorial Optimization. https://www.ingber.com/asa96_lessons.pdf.

89. Ingber, L.; Rosen, B. Genetic algorithms and very fast simulated reannealing: A comparison. *Mathematical Computer Modelling* **1992**, *16*, 87–100. https://www.ingber.com/asa92_saga.pdf.
90. Langouche, F.; Roekaerts, D.; Tirapegui, E. Discretization problems of functional integrals in phase space. *Physical Review D* **1979**, *20*, 419–432.
91. Langouche, F.; Roekaerts, D.; Tirapegui, E. *Functional Integration and Semiclassical Expansions*; Reidel: Dordrecht, The Netherlands, 1982.
92. Schulman, L. *Techniques and Applications of Path Integration*; J. Wiley & Sons: New York, 1981.
93. Ingber, L.; Fujio, H.; Wehner, M. Mathematical comparison of combat computer models to exercise data. *Mathematical Computer Modelling* **1991**, *15*, 65–90. https://www.ingber.com/combat91_data.pdf.
94. Ingber, L. Options on quantum money: Quantum path-integral with serial shocks. *International Journal of Innovative Research in Information Security* **2017c**, *4*, 7–13. https://www.ingber.com/path17_quantum_options_shocks.pdf.
95. Ingber, L.; Wilson, J. Statistical mechanics of financial markets: Exponential modifications to Black-Scholes. *Mathematical Computer Modelling* **2000**, *31*, 167–192. https://www.ingber.com/markets00_exp.pdf.
96. Ingber, L. Path-integral evolution of multivariate systems with moderate noise. *Physical Review E* **1995c**, *51*, 1616–1619. https://www.ingber.com/path95_nonl.pdf.
97. Ingber, L.; Wilson, J. Volatility of volatility of financial markets. *Mathematical Computer Modelling* **1999**, *29*, 39–57. https://www.ingber.com/markets99_vol.pdf.
98. Wehner, M.; Wolfer, W. Numerical evaluation of path-integral solutions to Fokker-Planck equations. I. *Physical Review A* **1983a**, *27*, 2663–2670.
99. Wehner, M.; Wolfer, W. Numerical evaluation of path-integral solutions to Fokker-Planck equations. II. Restricted stochastic processes. *Physical Review A* **1983b**, *28*, 3003–3011.
100. Wehner, M.; Wolfer, W. Numerical evaluation of path integral solutions to Fokker-Planck equations. III. Time and functionally dependent coefficients. *Physical Review A* **1987**, *35*, 1795–1801.